Turbulence Intensity Measurements in a Wind-Driven Mixed Layer

ERIC A. D'ASARO AND GEOFFREY T. DAIRIKI

Applied Physics Laboratory and School of Oceanography, University of Washington, Seattle, Washington

(Manuscript received 10 January 1996, in final form 3 March 1997)

ABSTRACT

Neutrally buoyant, high-drag floats were used to measure vertical velocity in the upper-ocean mixed layer during a period of rapid mixed layer deepening resulting from a storm. Salinity and temperature profiles, air–sea fluxes, and surface wave spectra were also measured. The location, Georgia Strait, British Columbia, is coastal with strong horizontal variability and may not be representative of the open ocean. The floats moved freely within the deepening mixed layer; the envelope of their motion corresponded closely to the extent of the mixed layer. The maximum vertical velocity was 0.12 m s^{-1}; the rms vertical velocity was about (0.02 m s^{-1})^2. The mean square vertical velocity, excluding surface waves, was 1.5–3.0 u_*^2, clearly higher than the upper bound of u_*^2 found in solid-wall turbulent boundary layers. The authors speculate that these anomalously high vertical velocities were due to Langmuir circulations generated by surface waves. These cannot occur in solid-wall boundary layers.

1. Introduction

The upper-ocean mixed layer is formed and maintained by turbulent mixing. Models of the mixed layer must successfully describe this mixing in order to predict the evolution of the mixed layer. Models proposed for this purpose vary greatly in dynamical assumptions. Most commonly, the models attempt to parameterize the turbulence and resulting mixing based on the rates of buoyancy and momentum exchange between the ocean and the atmosphere. Mellor and Yamada (1982), Kantha and Clayson (1994), and Gaspar et al. (1990), for example, simulate the statistics of the turbulence within the mixed layer using complex turbulence closure schemes based on a formal ''second-order closure'' of higher moments. Price et al. (1986) use a much simpler scheme, assuming infinitely fast turbulent mixing, which acts to relax static instability and low bulk or gradient Richardson numbers. Large et al. (1994) model the turbulence fluxes but not the turbulence and allow nonlocal and countergradient fluxes.

These models all ignore the presence of waves at the air–sea interface. This is a perilous assumption since surface waves are the most energetic features of the near-surface ocean. Surface waves are likely to be important for two reasons. First, wave breaking converts wave energy into turbulence and is thus an energy source for boundary layer turbulence (Agrawal et al. 1992; Melville 1996). Second, direct interactions between the waves and the turbulent velocities can transfer energy between them. The Craik–Leibovich theory (Leibovich 1983) shows how these interactions can produce ''Langmuir circulations,'' which efficiently mix the upper ocean. Li and Garrett (1993) study the properties of these circulations in detail and propose an upper-ocean model (Li and Garrett 1997) in which these circulations play a key role.

The development of mixed layer models has been greatly hindered by the lack of appropriate data. Time-varying profiles of temperature, salinity, and velocity through the mixed layer along with high-quality meteorological measurements have been made at a number of locations. Some time series of kinetic energy dissipation exist (e.g., Anis and Moum 1994; Brainerd and Gregg 1993a; Brainerd and Gregg 1993b), but no data on turbulence energy levels or fluxes exist. Thus, the recent attempts to improve model performance by Large et al. (1994) and Kantha and Clayson (1994) have relied heavily on analogs with atmospheric and laboratory boundary layers. Models developed and tested in this way may be blind to systematic differences in oceanic boundary layers due to the presence of surface waves.

In this paper, we describe preliminary measurements of mixed layer turbulence made with high-drag, neutrally buoyant floats in a rapidly deepening coastal mixed layer. The floats track the three-dimensional motion of water parcels as described by D'Asaro et al. (1996, henceforth DFOD). Linear surface waves have no pressure fluctuations along Lagrangian trajectories. The floats infer vertical velocity from pressure and are

Corresponding author address: Dr. Eric A. D'Asaro, Applied Physics Laboratory, University of Washington, 1013 N. E. 40th Street, Seattle, WA 98105-6698.
E-mail: dasaro@apl.washington.edu

therefore insensitive to the vertical velocity due to linear surface waves. Only very weak surface wave signals are, in fact, seen by the floats, and these are due mostly to the offset of the pressure sensor from the Lagrangian center of the float (see DFOD). The floats can therefore make accurate measurements of the small turbulent vertical velocities (centimeters per second) in the upper ocean even in the presence of very much larger vertical velocities (meters per second) due to surface waves.

In this paper we concentrate on measurements of turbulent intensity as measured by the squared vertical velocity $\langle w^2 \rangle$ during a single storm in Georgia Strait. Weller and Price (1988) measured very large (0.2 m s^{-1}) vertical velocities in the upper ocean and attributed these to Langmuir circulations. Mean square vertical velocities were not reported. Their Fig. 23, which summarizes both their observations and those of others, suggests an approximate correlation between the typical downwelling speed and wind speed. A value of $w_{\text{down}} = 0.1$ m s^{-1} corresponds to a wind speed of 10 m s^{-1}. This implies $w_{\text{down}}^2 \approx 70 u_*^2$.

The statistics of turbulence in neutral solid-wall turbulent boundary layers are well known. We consider only boundary layers on flat, that is, not curved but possibly rough walls. Laufer (1949) finds $\langle w^2 \rangle / u_*^2$ from 0.6 to 0.9 in the middle of an air-boundary layer at Reynolds number $U_0 L/\nu$ of 1.2×10^4 to 6×10^4. Here U_0 is the free-stream velocity, L is the approximate boundary layer thickness, and ν is the viscosity. McPhee and Smith (1976) made similar measurements under the arctic pack ice but at a much higher Reynolds number, about 10^7. They find $\langle w^2 \rangle / u_*^2$ ranging from 0.5 to 1.0, and profiles consistent with both laboratory and atmospheric boundary layer measurements. Cantwell (1981), reviewing the vast literature on this subject, states that the maximum value of $\langle w^2 \rangle / u_*^2$ found in laboratory measurements is about 1. In summary, solid-wall turbulent boundary layers have maximum values of $\langle w^2 \rangle / u_*^2$ of about 1 and boundary layer average values well below 1.

Thus, near-surface downwelling velocities in the upper ocean (i.e., Weller and Price 1988) are roughly 10 times larger than the rms velocities found in solid-wall boundary layers for the same stress. This is a remarkable difference, even considering that somewhat different quantities are being measured. In this paper, observations show $\langle w^2 \rangle / u_*^2 \approx 2.4$ with confidence limits that clearly exclude 1. These vertical velocities are larger than those in a solid-wall boundary layer for the same stress. We conclude that models of the upper ocean based on analogs with solid-wall boundary layers should be viewed with caution.

Section 2 describes the experimental location, the observations, and the data processing. Section 3 describes the evolution of the mixed layer stratification and turbulent intensity through the storm. Section 4 explores whether recent models of Langmuir circulations can explain the high turbulent intensity. Section 5 summarizes the results.

2. Data

a. Experimental location

Measurements were made in northern Georgia Strait, British Columbia, Fig. 1, in cooperation with David Farmer of the Institute of Ocean Sciences. Farmer et al. (1993) and McNeil (1995) describe the same events as this paper but concentrate on gas exchange. Farmer and Li (1995) analyze the near-surface patterns of bubble clouds and, from these, infer the horizontal structure of Langmuir circulations.

Georgia Strait is a deep (200–300 m) inland sea with an estuarine stratification and circulation (LeBlond 1983). A fresh surface layer varies seasonally in salinity with the flow of the Fraser River. Deeper, more saline, water is supplied from the Pacific Ocean, primarily from the south through Juan de Fuca and Haro Straits, but also from the north through Discovery Passage. The density stratification is almost entirely due to salinity, and the temperature variations are small. Tidal currents, the estuarine circulation, and smaller-scale eddies horizontally stir the freshwater from the Fraser River to produce large horizontal gradients in the stratification. During light winds, we typically observed horizontal variations in the surface density of 0.4–1 kg m^{-3} per kilometer, with much smaller variations at 30-m depth. Barotropic tidal currents in this region are 0.1–0.2 m s^{-1} (Crean 1978). Various floating and subsurface instruments deployed during our observations dispersed across the strait within a day of deployment, suggesting the presence of horizontal velocities of order 0.1 m s^{-1}. Large wire angles were commonly observed during CTD profiles, implying large vertical shears associated with the stratification.

This paper describes observations made on 22–25 November 1991 from the C.R.V. *Parizeau* through the passage of a storm. All times are local (PST = UTC − 8). The observations occurred within the shaded oval in Fig. 1. A time series of the positions of the ship and the various drifting instruments is not available. We will therefore deal only with the depth–time variability in the data, ignoring horizontal variability although realizing that it may be present.

b. Meteorological measurements

A Coastal Climate MINIMET buoy measured air temperature and vector-averaged wind speed and direction using an R. B. Young propellor–vane anemometer at 3-m height above the sea surface. Water temperature was measured a few tens of centimeters below the surface. Data were sampled every 2 minutes. We use the temperature data with the manufacturer's calibrations.

We estimate the error in the wind speed estimate as

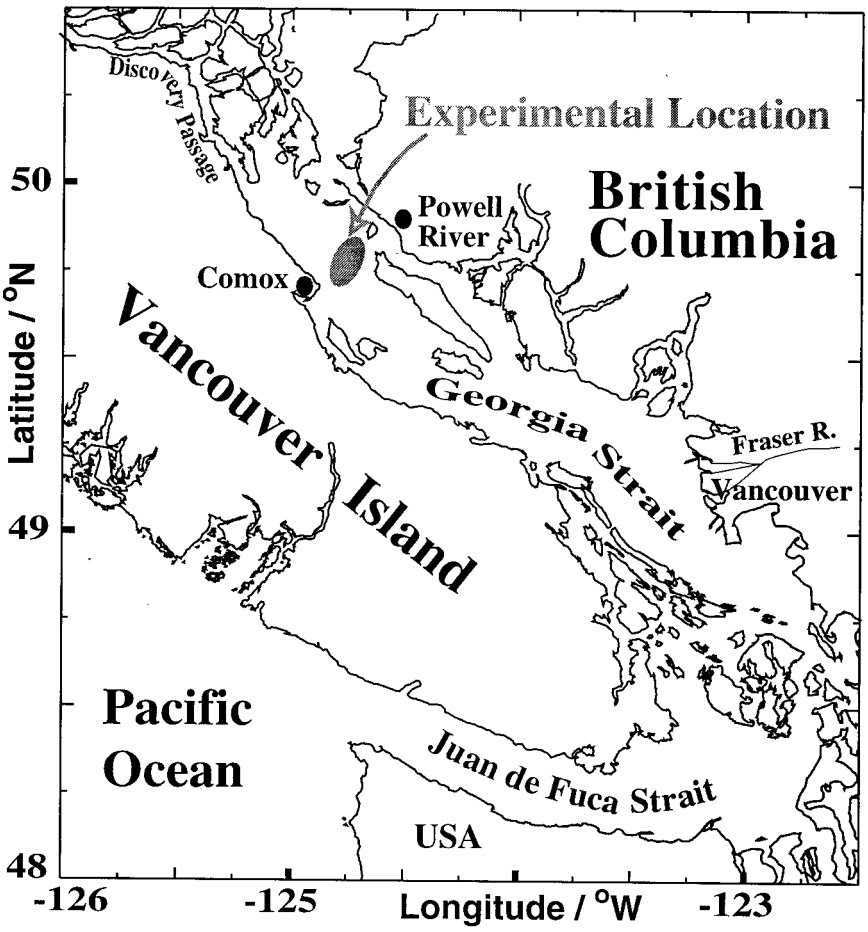

FIG. 1. Experimental location.

follows. The manufacturer quotes an error of 0.5 m s^{-1} or about 7% (0.5 m s^{-1} out of 7 m s^{-1}). Weller et al. (1983) find a considerably smaller error, about 1% from all sources, for a similar sensor mounted on a ship. We conservatively assume a 7% calibration error. The buoy was not properly ballasted and therefore did not remain upright, but tilted relative to the vertical owing to the surface waves. Using photographs, we estimate the average angle, θ, of the anemometer relative to the wind as about 18° at the height of the storm. We assume that this angle is proportional to the significant wave height and thus estimate its value throughout the storm. We divide the measured wind speed by $\cos(\theta)$ to obtain a corrected 3-m wind speed. The resulting time series of 3-m wind speed is plotted in the top panel of Fig. 2. This correction is small (about 5%) but inaccurate. We conservatively assign a 100% error to the correction or 5% of the wind speed.

On 24 November, the wind speed rises from about 1 m s^{-1} in the early morning to a peak of about 12 m s^{-1} at mid-day and then falls back to 1–2 m s^{-1} by midnight. The wind direction, not shown here, is steady at about 110°T, that is, from the SE, throughout the day. A plot of the wind speed and direction is given by Farmer et al. (1993).

c. Surface wave spectra

Surface waves were measured from upward-looking sonars on two very similar drifting, stable, subsurface platforms, SUSY (Vagle and Farmer 1992) and SEASCAN. SUSY was tethered to the meteorological buoy, while SEASCAN was left to drift freely. Each sonar measures the distance to the sea surface, which, corrected for the depth of the platform, gives a time series of the surface height every 0.5 s. Figure 3 shows the frequency spectra of wave height computed from 40-min segments of SEASCAN wave height data centered on approximately 0000, 0600, 0900, 1200, 1500, and 1800 PST 24 November. Each spectrum has been corrected for instrumental white noise, the level of which is determined for each spectrum from the level at 1 Hz. The spectra are truncated when the noise dominates the signal.

As expected, the waves grow in amplitude and their peak frequency decreases in response to the increased

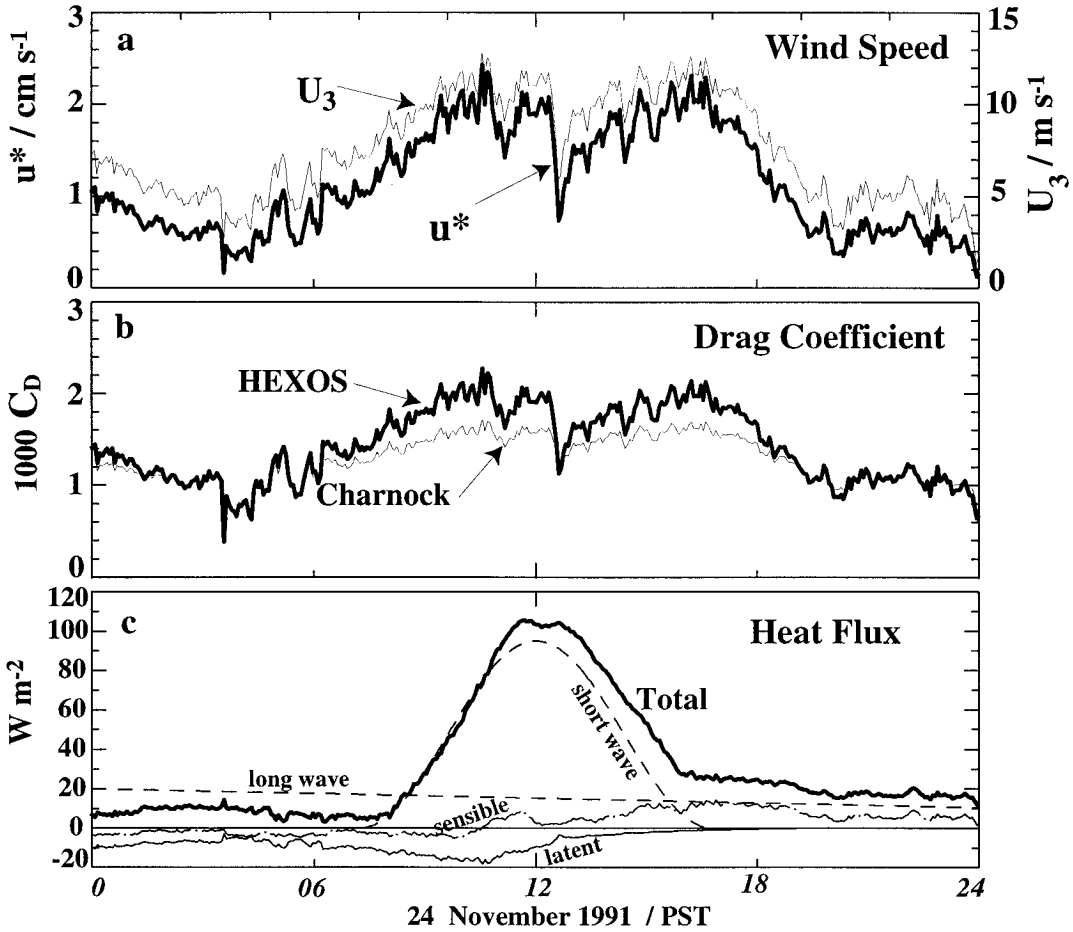

FIG. 2. Air–sea fluxes on 24 November 1991. (a) Three-meter wind speed corrected for buoy tilt (heavy curve) and friction velocity u_* (light curve) computed using the HEXOS (Smith et al. 1992) drag coefficient. Friction velocities are converted to values in water. Wind speed and u_* are not averaged in time. (b) Ten-meter drag coefficient computed using the Charnock relation (light curve) and HEXOS formulation (heavy curve). (c) Heat flux (heavy curve) and various components as labeled.

wind. At frequencies above the peak, the waves show a -4 spectral slope with a level that increases with u_*, consistent with the Phillips (1985) equilibrium range scaling. The same variations are seen in a more detailed time series of significant wave height (4 times the rms displacement) and peak wave frequency computed from the nearby SUSY sonar (Fig. 4).

d. Air–sea fluxes

The air–sea fluxes of heat and momentum were computed from the meteorological and wave measurements following the method of Large and Pond (1981) and Gill (1982) and are shown in Fig. 2. Radiation is the largest component of the heat flux. Longwave and shortwave radiation were estimated by interpolating between measurements at Comox and Powell River (see Fig. 1) (J. Gemmrich 1995, personal communication). Sensible and latent heat were computed from the air–sea temperature difference assuming 98% humidity at the surface and 94% at 10 m. These values were also chosen based on observations from Comox and Powell River. A value of $C_E = 1.5 \times 10^{-3}$ was used for the latent heat transfer coefficient. Values of $C_H = 0.83 \times 10^{-3}$ and 1.1×10^{-3} were used for the sensible heat transfer coefficient under stable and unstable temperature stratification, respectively. The heat flux warms the ocean throughout the entire period of interest. Note that this is different from the conclusions of Farmer et al. (1993) as they included only the heat flux into the top 5 cm. The heat flux is small, however, and its effects on the drag coefficient and on the upper-ocean temperature are minor.

Two different drag coefficients are shown in Fig. 2b. The first uses the Charnock relation, $z_0 = 0.011u_*^2/g$, relating the surface roughness z_0 to the wind stress. The coefficient, however, is appropriate for open ocean waves. Our waves are young, fetch limited, and thus rougher. We therefore used the HEXOS parameterization of surface roughness, $z_0 = 0.48u_*^3/(gC_p)$ (Smith et

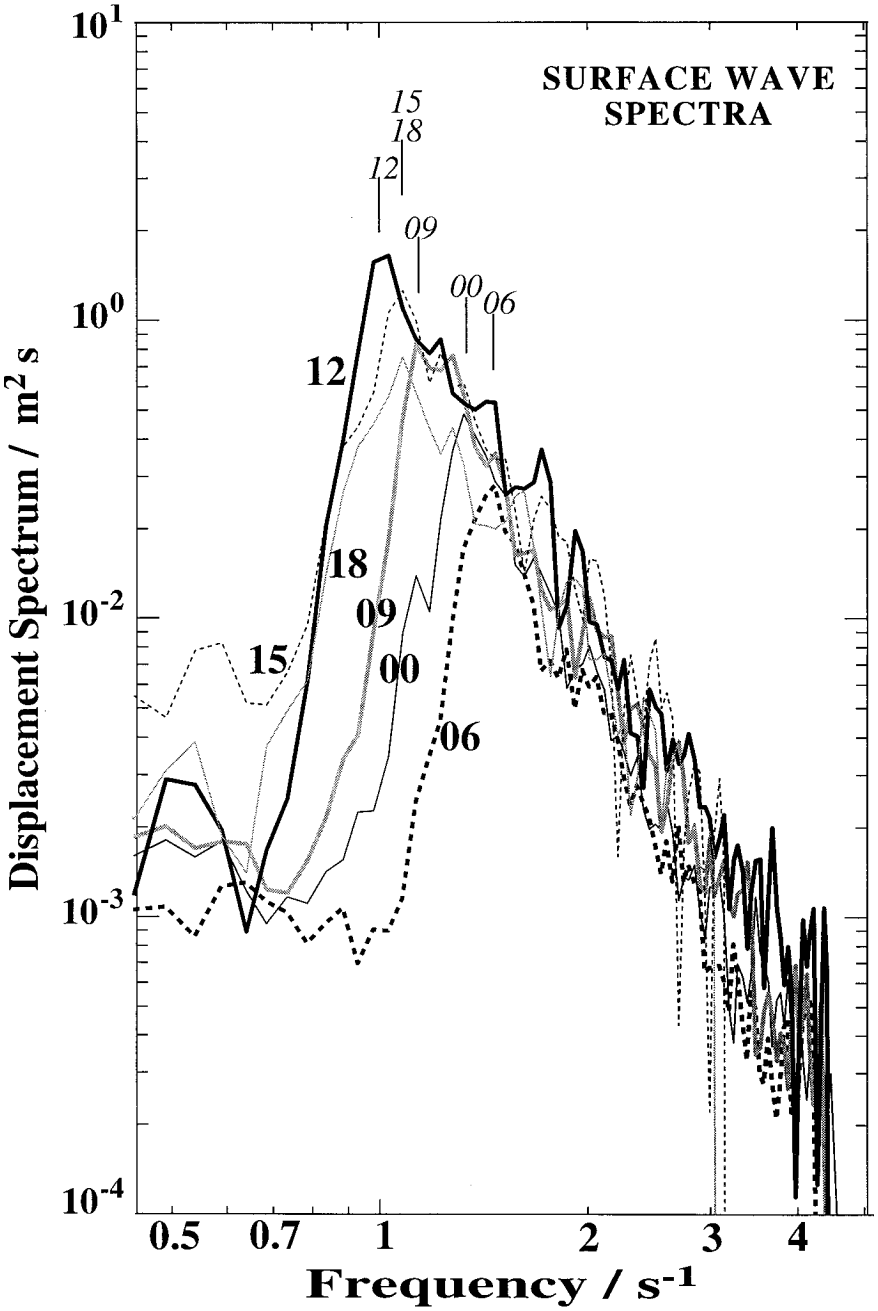

FIG. 3. Surface wave spectra. Labels indicate approximate hour of measurement (PST) on 24 November 1991. Labeled vertical line is location of peak for each spectrum.

al. 1992), where C_p is the phase speed of surface waves at the peak of the wave spectrum g/ω_{peak}. This yields a larger, and we believe, more realistic, drag coefficient. The resulting friction velocity is shown in Fig. 2a.

The error in our wind stress estimate is the sum of several factors. The uncertainty in the HEXOS surface roughness is about 20%; this leads to an uncertainty of about 5% in stress. The air–sea temperature difference changes the stress estimate by about 4%; the error in this is negligible. Buoy tilt and sensor calibration contribute errors of 10% and 14% respectively. Assuming the errors to be independent, we estimate the root of the sum of the squared errors as 18%. The sum of the errors is 29%. The largest error source is wind sensor calibration; our estimate may be unrealistically large.

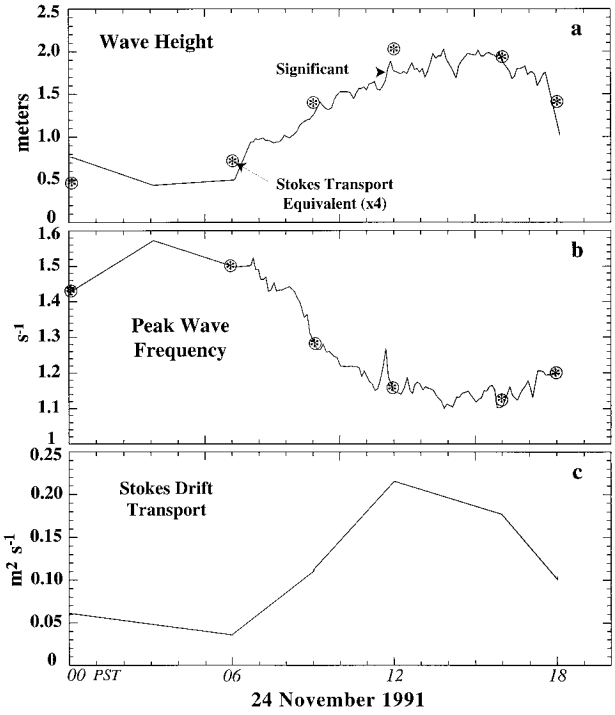

FIG. 4. Time series of wave properties. (a) Significant wave height (line) and four times the effective wave height for Stokes drift (circled stars). (b) Peak wave frequency (line) and peak wave frequency used in Stokes drift calculation (circled stars). (c) Stokes drift transport computed from spectra in Fig. 3.

e. CTD measurements and mixed-layer depth

Profiles of temperature, conductivity, and pressure were made from the C.R.V. *Parizeau* using an SBE-19 ''Seacat'' CTD, which was calibrated by the manufacturer (Sea-Bird Electronics) before and after the cruise. Typically, several casts were made at each station in order to resolve some of the small-scale variability. All of the potential temperature and density profiles are shown in Fig. 5 (light lines) along with the average for each station (heavy lines and shading). In addition, two CTDs were moored beneath the meteorological buoy along with additional temperature sensors. These are discussed by Farmer et al. (1993) and McNeil (1995).

A mixed layer is evident in each CTD profile. For each cast, the mixed layer depth was estimated as the depth at which density changed by 0.04 kg m^{-3} or potential temperature changed by 0.02°C from its first subsurface value. Mixed layer depths for each cast are plotted in Fig. 6c with ''+'' denoting depths estimated from temperature and ''O'' denoting depths estimated from potential density. In addition, two estimates of mixed layer depth from moored temperature sensors (McNeil 1995) are indicated by ''*''. Dashed lines indicate a subjective smoothing of these data to form a time series of mixed layer depth.

f. Lagrangian floats

Two neutrally buoyant Lagrangian floats were deployed in the mixed layer. These consist of a 1.5-m long, aluminum cylindrical hull, a 1-m diameter drag screen attached to the bottom of the cylinder, and recovery equipment. The floats are ballasted to have a buoyancy of only a few grams in seawater. In this deployment, they measured pressure and temperature. They are constructed to have a compressibility close to that of seawater so that their buoyancy does not change as they move vertically in a well mixed layer. They are constructed of aluminum and thus have a thermal expansion coefficient close to that of seawater. The combination of small buoyancy and high drag results in an instrument that follows the vertical and horizontal motion of the water to an accuracy of better than 1 cm s^{-1}. DFOD discuss the design of these floats in more detail, present examples of their water-following ability in this and other experiments, and provide a model of the float's accuracy.

Vertical velocity is computed from the 1-s pressure measurements by a first difference. Spectra of the resulting vertical velocity have a peak at about 0.01 s^{-1}, corresponding to the largest eddies. At frequencies above the peak, the spectra decay with the frequency^{-2} slope appropriate for a Lagrangian inertial subrange (see DFOD). At high frequencies pressure digitization noise is seen. The raw vertical velocity is averaged over 1 minute to remove this digitization noise.

Figure 6c shows depth–time trajectories of the Lagrangian floats on 23–25 November. The float deployments are identified by a letter, lower case before the storm and upper case during the storm. The number 2 or 3 indicates which float was used. This code is written just above the start of each trajectory. Figure 6b shows the vertical velocity for these same trajectories. Figure 7 shows the four float trajectories during the storm in more detail. Surface wave velocities are greatly attenuated in these data since pressure is constant along the Lagrangian trajectories produced by linear surface waves. A small surface wave signal is measured, however, because the pressure sensor, mounted in the top endcap, does not follow a Lagrangian trajectory. DFOD accurately model the measured float pressure spectra assuming that the pressure sensor is 1 m above a perfect Lagrangian trajectory in the known surface wave field. There is no evidence of non-Lagrangian behavior of the float at surface wave frequencies.

Ballasting of the Lagrangian floats was difficult on this cruise, both because of our relative inexperience (this was the first cruise with these floats) and because of the great horizontal variability in the upper ocean. In particular, in deployments B3 and C3 (Fig. 7) the floats appear to sink to below the mixed layer early in the record, suggesting that their density was up to 0.1 kg m^{-3} heavier than that of the mixed layer. Multiplying by the float's volume of 20 L, we estimate that the float

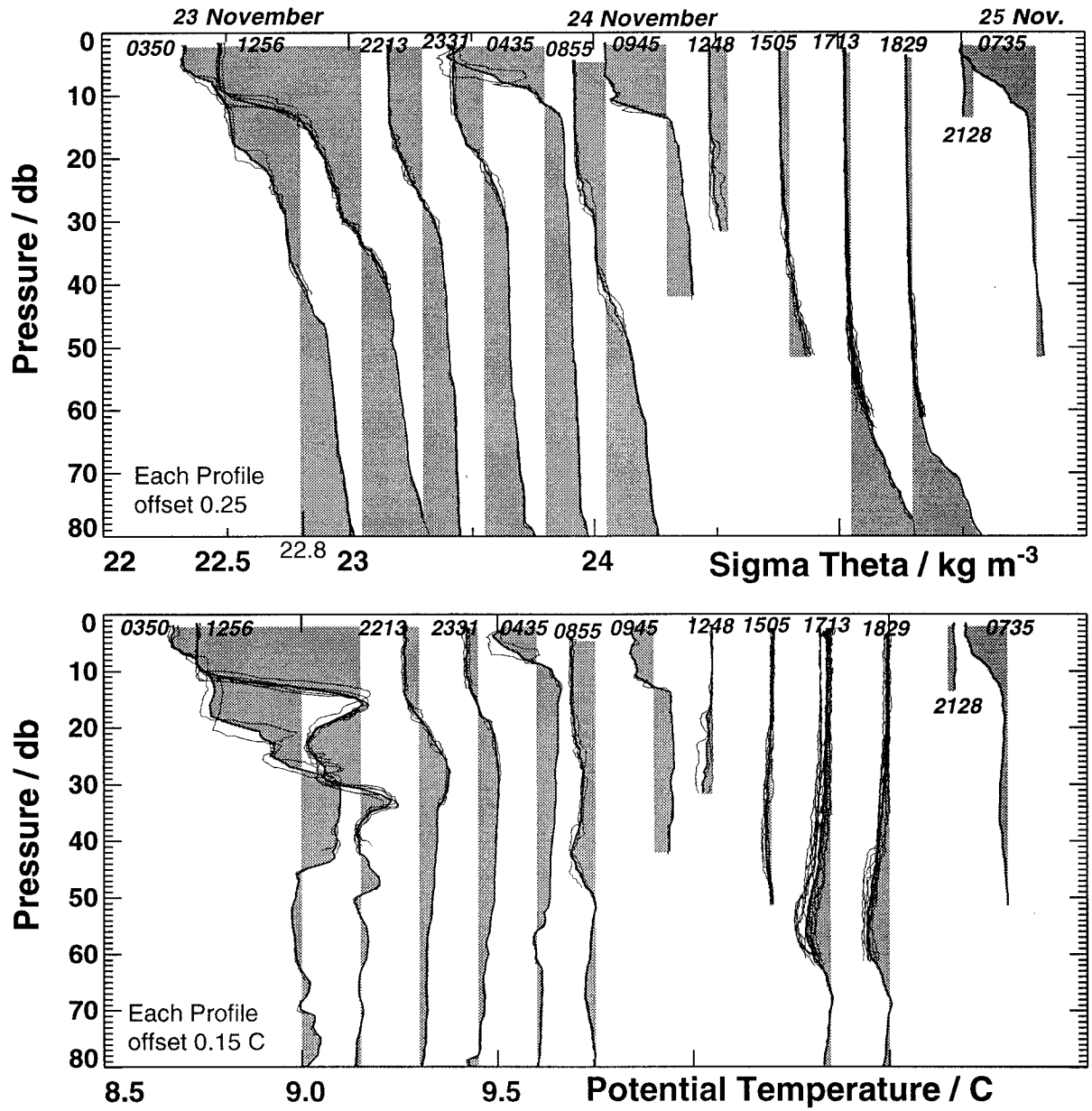

FIG. 5. Profiles of potential density (top) and temperature (bottom) made from the C.R.V. *Parizeau.* The profiles at each station are shown by the light lines, and the average of all the profiles by the heavy lines and shading. The shading is centered on 22.8 σ_θ (top) and 9.0°C (bottom). The profiles are offset 0.25 σ_θ (top) and 0.15°C (bottom). Each group of profiles is labeled at the top with the time at which it ended.

was up to 2 g heavy in the mixed layer. Knowing the float's drag coefficient, we estimate a downward fall rate of 5 mm s^{-1}, or 18 m h^{-1}. This seems consistent with the initial sinking rate of B3. The typical vertical velocities in the mixed layer are several centimeters per second, significantly larger than the downward bias due to the ballasting. This is consistent with the eventual entrainment of both B3 and C3 back into the mixed layer. These ballasting errors, although they produce a bias in the float's average depth toward the top or bottom of the mixed layer, have a small effect on $\langle w^2 \rangle$. The maximum bias velocity due to misballasting (5 mm s^{-1}) will increase the typical value of $\langle w^2 \rangle$ during the storm (20 mm s^{-1}) by only 6%. The effects could be larger during the periods of low winds at the beginning and end of the storm. However, these trajectories (A3 and D3) show well-ballasted floats (Fig. 6) and have values of $\langle w^2 \rangle / u_*^2$ that show no evidence of being abnormally high.

The float is insensitive to velocities smaller than itself. The measured value of $\langle w^2 \rangle$ is less than the true value since the variance in the small-scale motions is not in-

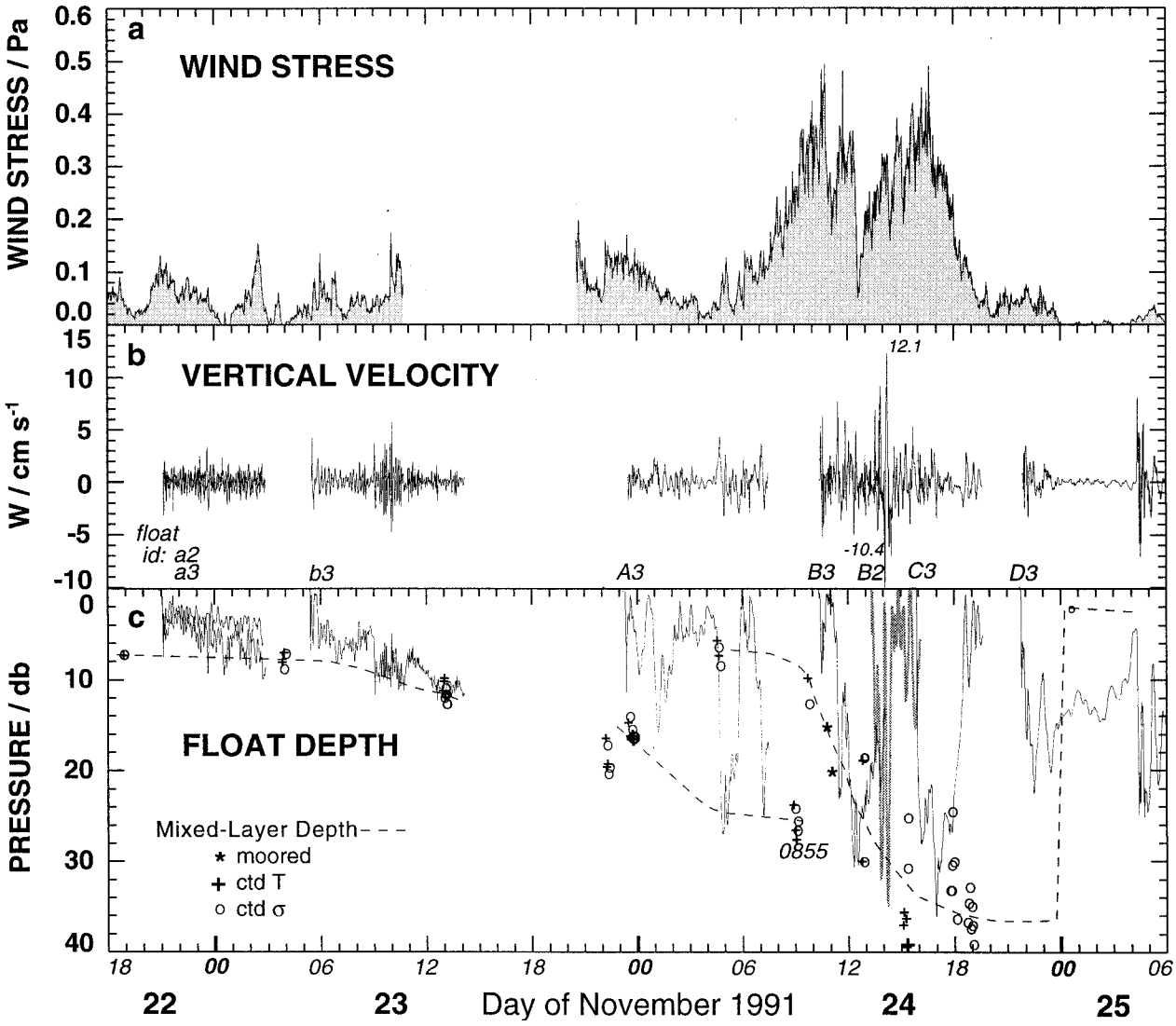

FIG. 6. Summary of Lagrangian float data. (a) Wind stress from HEXOS u_* in Fig. 2. (b) Vertical velocity measured from vertical displacement of floats. The maximum up and down velocities are marked. (c) Depth of floats. Float ID is written above top axis at start time of each float trajectory. Mixed layer depths, deduced from CTD data, are indicated by the symbols. Dashed lines give interpolated, smoothed mixed layer depth. Two mixed layer depths are indicated for the morning of 24 November, indicating horizontal variability between the location of float A3 and the rest of the data.

cluded. DFOD present a model of this effect based on the shape of the observed spectra of vertical velocity. The fraction of vertical velocity variance lost is about $(L/H)^{2/3}$, where L is the effective float size, somewhat less than 1 m, and H is the mixed layer depth, about 20 m. This predicts that the finite size of the float will decrease $\langle w^2 \rangle$ by about 10%. Effects of misballasting and float size are therefore opposite and of similar magnitude. The net effect is probably a small underestimate of $\langle w^2 \rangle$. We have not corrected for this.

The temperature at the top of the float was measured using the same electronics board and thermistor used in Sea-Bird Electronics deep-ocean CTDs. Unfortunately, the thermistor was embedded in the top endcap, giving it a complex relationship to the water temperature. Luckily, we obtained an accurate measurement of the response function each time the float was transferred from the warm laboratory on the ship to the much colder ocean. The thermistor response is dominated by an exponential decay with a 21-s time constant. This accounts for more than 90% of the temperature change. Temperature fluctuations with timescales longer than 100 s therefore have a small error. Other components of the response function have longer time constants and smaller amplitudes. Since the change in temperature associated with the immersion of the float in the water is much larger (1°–10°C) than the temperature fluctuations within the water (0.01°C), the transient temperature re-

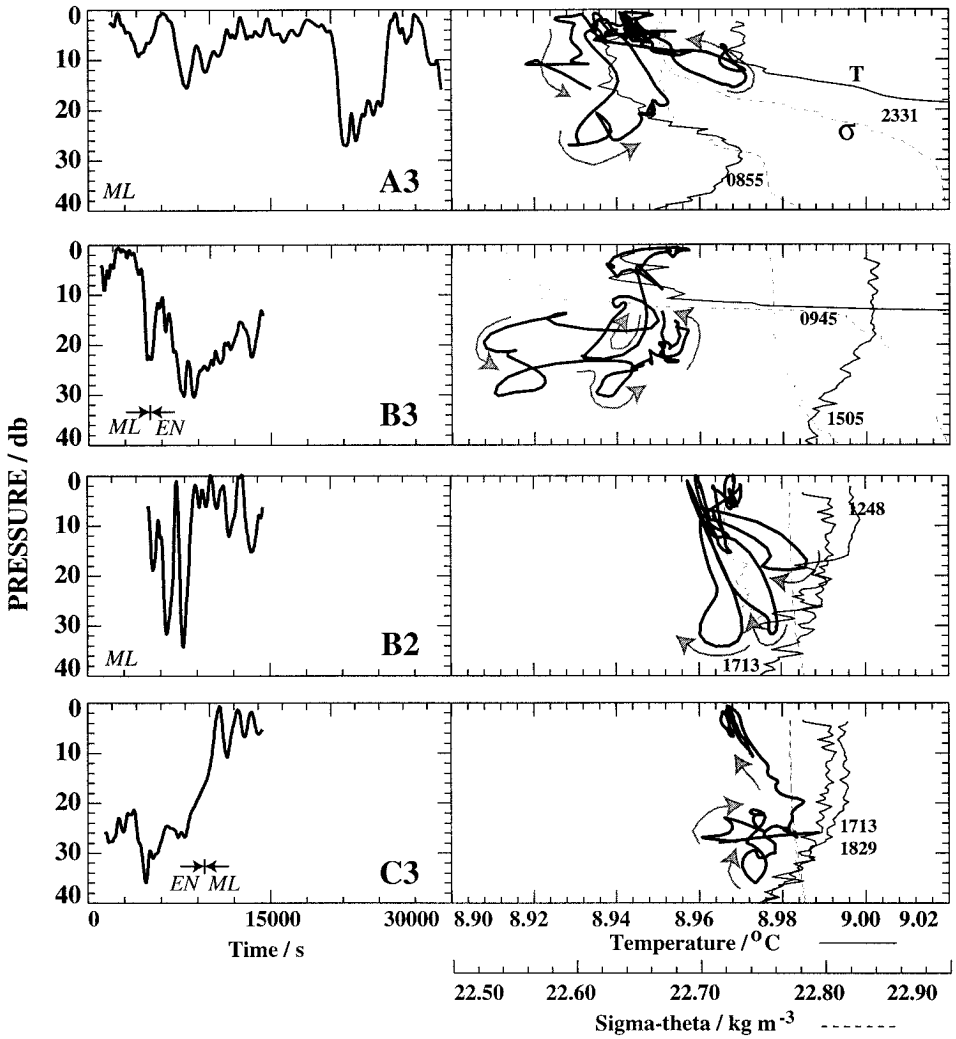

FIG. 7. Temperature and depth data from Lagrangian floats deployed during the storm. The left panel shows the depth/time trajectory for each float, enlarged from Fig. 6. Time is in seconds from immersion in water. The first 500 s are not shown since the temperature has not yet recovered from the large change due to immersion. The labels *ML* and *EN* indicate classification of trajectories as mixed layer or entrainment zone. The right panel shows the depth/temperature trajectory (heavy line) for the float, with gray arrows to indicate the direction. Temperature is corrected for the immersion transient as described in the text. Average temperature (light line) and σ_θ (dashed light line) for CTD profiles taken near the start and end of the deployment are shown. The name of each profile is its end time. No CTD data were taken at the end of C3, so CTD 1829, taken at the middle of the trajectory, is shown. Note that the float and CTD temperatures are different owing to both calibration errors and spatial variability in the upper ocean.

sponse due to the immersion overwhelms the oceanic signal for over an hour afterward. We correct for this by subtracting a single exponential from each temperature record with a time constant that varies between 600 s and 1000 s and an amplitude that varies from 0° to 0.4°C. The first 500 s of temperature data are discarded as inaccurate. The data have an error due to the immersion transient that decays exponentially with time and equals about 0.015°C at 500 s. An approximate temperature calibration of the floats was made before the cruise. Float 2's temperature was adjusted from this value by 0.13°C to agree with the temperatures measured by float 3. After this correction both floats agreed with the moored and profiling CTDs to within 0.1°C when the measurements were nearby and within the mixed layer. The difference between the CTD and float temperatures is apparent in Fig. 7. The temperature fluctuations are probably accurate to at least 0.01°C.

3. Analysis and results

a. Mixed layer evolution

Figure 6 summarizes the evolution of the mixed layer. Before the storm (22–23 November) the wind stress is

less than 0.1 Pa, and the mixed layer is less than 10 m thick. Three floats deployed during this period (A2, A3, and B3) remain in the mixed layer and oscillate vertically. The mixed layer depth is not much larger than the size of the floats, making the interpretation of the trajectories difficult. The floats' vertical motion is undoubtedly strongly influenced by internal waves propagating on the strong pycnocline beneath the mixed layer. The spectrum of vertical velocity computed from float trajectory A3, for example, exhibits a strong peak at a frequency just below the maximum buoyancy frequency in the pycnocline, about 0.03 s^{-1}.

As the wind stress increases on 24 November, the mixed layer increases in depth. The mixed layer depth as determined by density (circles in Fig. 6) is shallower than that determined by temperature (pluses in Fig. 6). The dashed line, our best estimate of the mixed layer depth, is biased toward the density-determined value. Difficulties arise, however. CTD 0855 (labeled in both Figs. 5 and 6), taken at the end of the trajectory of float A3, shows a mixed layer 26 m deep. CTD 0945, taken at SUSY, 50 minutes later and 7 n mi away, shows a mixed layer 7 m deep. Since CTD 0945 is consistent with the other CTD measurements made near SUSY, we explain this discrepancy as the result of horizontal variability. This interpretation is supported by the float data. Float A3 moves vertically in the water between the surface and about 25 m. This is consistent with the mixed layer depths measured at the beginning (CTDs 2213 and 2331) and end (CTD 0855) of the trajectory. Similarly, the trajectories of floats B3, B2, and C3, taken together, show vertical motion extending to a depth that closely follows that of the mixed layer. Two time series of mixed layer depth are therefore shown in Fig. 6, one at SUSY, which includes CTD 0945, and one associated with float A3, which includes CTD 0855. Additional unresolved horizontal variability undoubtedly exists in this area.

After the storm, on 25 November, the single CTD profile (0735) shows a shallow or nonexistent mixed layer. The moored CTD and temperature data (McNeil 1995) show that this restratification happens rapidly and is associated with oscillations in temperature. Similarly, float D3 settles to about 14 m after the storm ends; then, at about 0400, it rises and then suddenly plunges downward to about 22 m, oscillating rapidly in the vertical before settling out again. These observations suggest that the restratification occurs through the passage of an internal bore.

Our data can only describe the one-dimensional, depth–time evolution of the upper ocean, yet three-dimensional effects are clearly present. McNeil (1995) computes the heat and salt budgets of the mixed layer during the period of rapid deepening (0900–1800) on 24 November and concludes that a one-dimensional model explains much of the observed changes in mixed layer heat and salt content. On longer timescales, this is clearly not true; the heat and salt contents of the CTD profiles in Fig. 5 are not constant. In particular, the 22.8-σ_θ isopycnal rises about 28 m in the 24 hours from 0350 23 November to 0435 24 November, resulting in a large increase in the salt content of the upper 40 m. Similarly, the surface density decreases about 0.25 kg m^{-3} between CTD 2126 on 24 November and CTD 0735 on 25 November, presumably owing to restratification associated with the bore. During the short period of maximum wind, however, a one-dimensional approach is probably appropriate.

Additional evidence of one-dimensional deepening is present in the float temperature data. Two periods of rapid mixed layer deepening occur in these data. The first is early in the morning of 24 November along float trajectory A3, which links CTDs 2331 and 0855 (Figs. 6c, 7). The second occurs later the same day a few kilometers away and is described by the CTD and float trajectories during this time (Figs. 6c and 5). In the first event, the mixed layer is colder than the underlying water and cools as the mixed layer deepens. In the second event, the mixed layer is initially colder than the underlying water (CTD 0945), but later becomes slightly warmer (CTDs 1248–1713), presumably owing to the combination of solar heating and advection.

From an Eulerian viewpoint, the mixed layer grows through the action of turbulent fluxes of heat and salt. These change the temperature and salinity of both the mixed layer and the layers undergoing entrainment. From a Lagrangian viewpoint, the fluxes must be carried by the exchange of water molecules between the mixed layer and the entraining layers and the eventual incorporation of nearly all molecules from the entrainment region into the mixed layer.

Such exchanges are evident in the temperature records of the floats (Fig. 7). Floats A3 and B2 remain in the mixed layer during the two rapid deepening events. They cycle between the mixed layer and the entrainment region, moving deeper on each pass as the mixed layer deepens. Changes in the temperature measured along a Lagrangian trajectory imply heating or cooling of the surrounding water by mixing. The measured changes are indeed consistent with entrainment of water by the mixed layer. Float A3 warms at the bottom of each loop since the entrainment region is warmer than the mixed layer during the first deepening event. Similarly, float B2 cools since the deeper water is cooler in the second event. On each pass, therefore, each float leaves the entrainment region (going up) with a different temperature than when it entered the region (going down). This implies a net vertical heat flux in the water. The pattern is particularly clear for float B2. Each of the three loops shows further cooling and deepening of the mixed layer and the breakdown of its residual stratification.

b. Turbulent intensity

The major goal of this paper is to compare average squared mixed-layer vertical velocity $\langle w^2 \rangle$ and friction velocity u_*^2. Two timescales are relevant. The wind

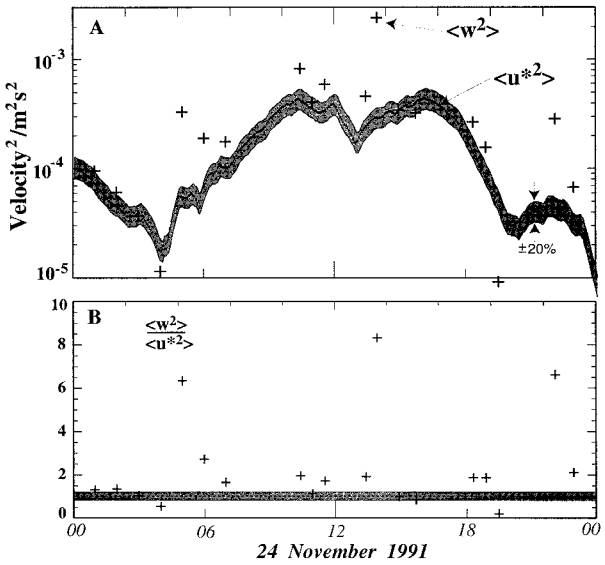

FIG. 8. (a) Rms vertical velocity. The pluses show the 1-h average value of squared vertical velocity. The dots show u_*^2 computed from 1-h average winds. The shaded region shows the estimated error in u_*^2. (b) Ratio of 1-h average w^2 to 1-h average u_*^2. The mean of these values is above 1.

stress, and thus u_*^2, is computed with 1-h averages, this being the approximate averaging time used in computing the HEXOS surface roughness and thus our drag coefficient. The correlation time of w in these data is 150–300 s; we will assume 300 s.

The most conservative estimate of $\langle w^2\rangle/u_*^2$ uses 1-h averages for both quantities and regards each $\langle w^2\rangle$ estimate as independent. The resulting $\langle w^2\rangle$ values (pluses) and u_*^2 (dots) are plotted in Fig. 8a. The ratio $\langle w^2\rangle/\langle u_*^2\rangle$ is plotted in Fig. 8b. Only data from the mixed layer, that is, the ''ML'' segments in Fig. 7, are used. Estimated error bounds on u_*^2 (20%) are shown as the shaded band. It should be evident from Fig. 8b that $\langle w^2\rangle/u_*^2$ is larger than 1.

Statistical tests confirm this. Our null hypothesis is that $\langle w^2\rangle/u_*^2$ equals 1. Given a 20% uncertainty on u_*, $\langle w^2\rangle/u_*^2$ must be larger than 1.2 for this to be true. Using 1-h averages, the average value of $\langle w^2\rangle/u_*^2$ is 2.2. The bootstrap method (Efron and Gong 1983) yields 95% confidence limits of 1.4–3.0. We can gain more degrees of freedom by shortening the averaging interval for $\langle w^2\rangle$. The smallest defensible averaging for which the estimates are independent is the correlation time of 300 s. Using this but maintaining 1-h averaging for the wind speed yields a mean of 2.4 and 95% bootstrap confidence limits of 1.8–2.7. With no averaging, the $\langle w^2\rangle$ estimates are correlated, and the 819 samples have only 163 degrees of freedom. Their mean is 2.5, and the Gaussian 95% confidence limits are 1.7–3.3. In all cases, the lower 95% confidence limit is well above 1.2; in all cases, the probability of $\langle w^2\rangle/u_*^2$ being 1 or less is well below 5%.

In Fig. 8a there are 19 data points; 12 lie above the u_*^2 error bounds, 2 lie below, and 5 are within the error bounds. Distributing these 5 equally above and below yields 4.5 points below and 14.5 above. The probability of 4.5 positive results in 19 tries given an equal probability of positive and negative results is about 2%. The probability of $\langle w^2\rangle/u_*^2$ being 1 or less is low.

There is a high probability that $\langle w^2\rangle/u_*^2$ is larger than 1 in these data. Furthermore, the analysis has probably biased our estimate of $\langle w^2\rangle/u_*^2$ low for several reasons. First, w^2/u_*^2 is quite intermittent. For example, half of the contribution to the mean is due to the 6% of the values above 10. The shape of the pdf indicates that we have undersampled these large values of w, implying that our computed mean is probably low. Smoothing the pdf, which partially corrects for the intermittency, can easily raise the mean from 2.4 to 3.0. Second, our 20% error estimate on u_*^2 is probably excessive. This lowers the estimated probability that $\langle w^2\rangle/u_*^2$ is larger than 1 within the error bounds. Third, we have used the larger of two possible drag coefficients and applied a large tilt correction to the wind speed. These choices drive the value of $\langle w^2\rangle/u_*^2$ down. Finally, the value of $\langle w^2\rangle$ computed from the floats is probably low owing to the combined effect of misballasting and the finite size of the float.

Recently, we have collected several weeks of similar data in the wintertime, North Pacific ocean. Preliminary analysis indicates that $\langle w^2\rangle/u_*^2$ is larger than 1 in these data also.

4. Discussion

a. The wave vortex force

The major result of this paper is the observation of anomalously large vertical velocities in a wind-wave-forced upper-ocean boundary layer. Surface waves, which are not present in solid-wall boundary layers, are an obvious candidate to explain the larger turbulent intensities.

Surface waves can generate motions in the mixed layer through the wave vortex force (Leibovich 1983)—that is, Langmuir circulations. Directional surface waves with a Stokes drift $u_s(z)$ induce an additional force $u_s \times \mathbf{\Omega}$ on the wave-averaged currents, where $\mathbf{\Omega}$ is the vector vorticity of the averaged currents. This results in the generation of vorticity that is aligned with the wind stress direction and a cross-wind circulation consisting of counterrotating vortices.

b. Equations

Li and Garrett (1993) analyze the resulting equations and show that, in the absence of stratification, they depend on two nondimensional numbers: a Langmuir number

$$La = \left(\frac{\nu\beta}{u_*}\right)^{3/2}\left(\frac{u_*}{S_0}\right)^{1/2}, \quad (1)$$

where ν is an eddy viscosity, and the ratio u_*/S_0. A monochromatic surface wave field is assumed. It has a surface displacement $ae^{\beta x-\omega t}$ and thus the Stokes drift profile

$$u_s(z) = 2S_0e^{2\beta z}, \quad (2)$$

where $S_0 = a^2\beta\omega$ is half the surface value of the Stokes drift and $\omega^2 = g\beta$. Note that there are other nondimensional parameters, involving time and domain size, which may be important.

c. Parameters

Values of u_*, S_0, β, and ν are needed to compare this model with our data. The wind stress (Fig. 6) provides u_*. Li and Garrett (1993) treat ν as an eddy viscosity and show that their results are relatively insensitive to its value. We use $\nu = 0.01$ m^2 s^{-1}. This implies $La = 0.046$, which is in the center of the range of values used by Li and Garrett (1993). The values of S_0 and β are determined from the wave spectra in Fig. 3 by finding values that best match the total Stokes transport, that is, the depth integral of $u_s(z)$ and the shape of $u_s(z)$. The total transport is computed from the spectra. We assume a $\cos^5$ directional spectrum based on directional wave spectra computed from the sidescan sonar on SUSY (M. Trevorrow 1994, personal communication). The results are plotted in Fig. 4c. The spectra are accurately described by a -4 spectral slope with a low-frequency cutoff ω_0. The Stokes drift for such a spectrum has the shape of an exponential integral $E_1(-2k_0z)$, where $gk_0 = \omega_0^2$. The functional form can be approximated by an exponential decay in the region that contributes most to the total transport; a value of $\beta = 2k_0$, and thus $\omega = 2^{1/2}\omega_0$, matches the first moments of the depth distribution of Stokes transport for the exponential and exact functional forms. The value of S_0 is then chosen so that the total Stokes transport of the exponential matches the known value. This produces the time series of Stokes transport, peak frequency, and effective Stokes wave height shown in Fig. 4a.

We will consider the period of nearly constant wind stress extending from 0900 to about 1800. The average value of u_* is about 0.016 m s^{-1} and the average value of S_0 is about 0.045 m s^{-1}, so the ratio S_0/u_* is about 2.7. This is well outside of the range of 4.6 to -6.9 found by Li and Garrett (1993) based on open-ocean data, presumably because the short fetch in Georgia Strait leads to small, rough waves and thus a high u_* and low S_0. The surface heat flux is not important dynamically (Li and Garrett 1997), but affects the temperature field.

d. Two-dimensional models

Most discussions of Langmuir circulations are two-dimensional. Figure 8 of Li and Garrett (1993) shows profiles of vertical velocity in well-developed, two-dimensional Langmuir cells. Given their figure, their nondimensionalization, and the above values of La and S_0/u_*, we estimate a depth-average $\langle w^2\rangle/u_*^2$ of 0.68. We have also run 2D Langmuir cell simulations with our own code, which has a somewhat different box size, grid, and numerical algorithmn from that of Li and Garrett (1993) and that does not achieve a steady state in the 9 h from 0900 to 1800. A test problem run with both our code and the Li and Garrett (1993) code demonstrates that the two codes give nearly the same result for the same problem. Our simulation yields a depth average $\langle w^2\rangle/u_*^2$ of 0.5. Both values are clearly below 1.0 and do not agree with the observations. Perhaps these simple models should not be expected to model all of the velocity variance in the mixed layer, only that due to Langmuir circulations. Perhaps they therefore get the mixing rates right, but not the velocity variance. Nevertheless, they predict vertical velocities that are not very energetic compared to these observations.

e. Three-dimensional models

More realistic simulations of the observations might be expected from three-dimensional models. Skyllingstad and Denbo (1995) and McWilliams et al. (1997) describe three-dimensional, large eddy-resolving (LES) models of the upper-ocean mixed layer that include the Craik–Liebovich vortex force. McWilliams et al. (1997) also include advection by the Stokes drift. Both models use a subgrid parameterization that attempts to model the effect of turbulent motions at unresolved scales. To the extent that this is done accurately, the effective Langmuir number of these simulations is very large and the only important nondimensional parameter is S_0/u_*. McWilliams et al. (1997) call $(2S_0/u_*)^{-1/2}$ the ''Turbulent Langmuir number.'' With $S_0/u_* = 0$ these simulations have no surface waves and approximately duplicate the results of solid-wall turbulent boundary layers.

Both Skyllingstad and Denbo (1995) and McWilliams et al. (1997) find large increases in $\langle w^2\rangle/u_*^2$ when the vortex force is used. With no waves, McWilliams et al. (1997) find $\langle w^2\rangle/u_*^2$ of about 0.4 averaged across the mixed layer. With waves, this increases to about 1.4. Similarly, Skyllingstad and Denbo (1995), in their ''MILDEX'' simulation with waves, find $\langle w^2\rangle/u_*^2$ of about 2.0. A preliminary run of the same model tuned to our data ($\tau = 0.26$, $S_0/u_* = 2.7$) yields a mixed layer average $\langle w^2\rangle/u_*^2$ of 2.0 (E. Skyllingstad 1995, personal communication) and peak vertical velocities of 0.11 m s^{-1}. Both of these values are close to our observations. This suggests that the anomalously

high values of $\langle w^2 \rangle / u_*^2$ found in the data may be due to the vortex force or, in a broad sense, Langmuir circulations.

5. Summary

Measurements of upper-ocean turbulence during rapid mixed layer deepening were made using neutrally buoyant floats, supported by CTD, surface wave, sonar, and air–sea flux data. The location, Georgia Strait in British Columbia, exhibits strong horizontal variability in stratification and mixed layer deepening.

The data reveal the following features:

- The mixed layer deepens from 5 m to about 30 m during the storm, and restratifies within 10 h of the end of the storm. The mixed layer deepens much sooner at a second location 13 km away.
- The neutrally buoyant floats move freely within the mixed layer, with maximum vertical velocities of 0.12 m s^{-1} downward and 0.10 m s^{-1} upward.
- The ratio of the mean square mixed layer vertical velocity, $\langle w^2 \rangle$, to the wind stress, u_*^2, is about 2.3 with 95% confidence limits of about 1.5–3.0. The probability of this ratio being 1 or less is a few percent.

These results are compared with the predictions of various proposed models of the upper-ocean boundary layer.

- Models tuned to noncurved, solid-wall turbulent boundary layers such as those commonly studied in the laboratory, under pack ice, or in the lower atmospheric will predict $\langle w^2 \rangle / u_*^2$ less than 1. This is inconsistent with the observations.
- The two-dimensional, low-resolution Langmuir cell model of Li and Garrett (1993) driven by the measured wind stress and wave field predicts $\langle w^2 \rangle / u_*^2$ of about 0.5. This is inconsistent with the observations.
- The three-dimensional, ''large-eddy'' simulations of Skyllingstad and Denbo (1995) and McWilliams et al. (1997), which include the Craik–Leibovich wave vortex force (Leibovich 1983), predict $\langle w^2 \rangle / u_*^2$ in the range of 1.4–2. The values are similar to those found in these data.

The results suggest that the anomalously large vertical velocities found in the data may be due to the action of surface waves, through the Craik–Leibovich wave vortex force. Less precisely, the data suggest that Langmuir circulations, which are present in the ocean but not in wall-bounded boundary layers, may be responsible for the large vertical velocities found in these data.

Acknowledgments. We would like to thank David Farmer and his group for a long standing, pleasant, and highly productive collaboration, which included the gathering of these data. The captain and crew of the C.R.V. *Parizeau* kept the ship operating, and thus enabled the success of this effort, despite injury, steering failures, and bad weather. Dr. T. Boyd helped greatly in collecting the data at sea; T. Lehman and J. Osse were instrumental in preparing the floats. This work was supported by ONR Grants N00014-90-J-1253, N00014-94-l-0024, and N00014-93-l-1085 and NSF Grants OCE9301835 and OCE9213915 to the University of Washington, and by ONR Grants 91-J-1964 and 90-J-1443, Canadian National Science and Engineering Council grants, and the Panel on Energy Research and Development Grant 6B2005, all to the Institute of Ocean Sciences.

REFERENCES

Agrawal, Y., E. Terray, M. Donelan, P. Hwang, A. Williams III, W. Drennan, K. Kahma, and S. Kitaigorodski, 1992: Enhanced dissipation of kinetic energy beneath surface waves. *Nature,* **359** (6392), 219–220.

Anis, A., and J. Moum, 1994: Prescriptions for heat flux and entrainment rates in the upper ocean during convection. *J. Phys. Oceanogr.,* **24,** 2142–2155.

Brainerd, K., and M. Gregg, 1993a: Diurnal restratification and turbulence in the oceanic surface mixed layer. Part I: Observations. *J. Geophys. Res.,* **98,** 22 645–22 656.

——, and ——, 1993b: Diurnal restratification and turbulence in the oceanic surface mixed layer. Part II: Modeling. *J. Geophys. Res.,* **98,** 22 657–22 664.

Cantwell, B., 1981: Organized motion in turbulent flow. *Annu. Rev. Fluid Mech.,* **13,** 457–515.

Crean, P., 1978: A numerical model of barotropic mixed tides between Vancouver Island and the mainland and its relation to studies of the estuarine environment. *9th Int. Liege Symp. on Ocean Hydrodynamics, Hydrodynamics of Estuaries and Fjords,* J. C. J. Nihoul, Ed., Elsevier, 283–314.

D'Asaro, E., D. Farmer, J. Osse, and G. Dairiki, 1996: A Lagrangian float. *J. Atmos. Oceanic Technol.,* **13,** 1230–1246.

Efron, B., and G. Gong, 1983: A leisurely look at the bootstrap, the jackknife and cross-validation. *Amer. Stat.,* **37,** 36–48.

Farmer, D., and M. Li, 1995: Patterns of bubble clouds organized by Langmuir circulation. *J. Phys. Oceanogr.,* **25,** 1426–1440.

——, C. McNeil, and B. Johnson, 1993: Evidence for the importance of bubbles in increasing air-sea gas flux. *Nature,* **361,** 620–623.

Gaspar, P., Y. Gregoris, and J.-M. Lefevre, 1990: A simple eddy kinetic energy model for simulations of the oceanic vertical mixing: Tests at station PAPA and long-term upper ocean study site. *J. Geophys. Res.,* **95,** 16 179–16 193.

Gill, A. E., 1982: *Atmosphere–Ocean Dynamics.* Academic Press, 662 pp.

Kantha, L., and C. Clayson, 1994: An improved mixed layer model for geophysical application. *J. Geophys. Res.,* **99**(C12), 25 235–25 266.

Large, W., and S. Pond, 1981: Open ocean momentum flux measurements in moderate to strong wind. *J. Phys. Oceanogr.,* **11,** 324–336.

——, J. McWilliams, and S. Doney, 1994: Oceanic vertical mixing: A review and a model with a nonlocal boundary layer parameterization. *Rev. Geophys.,* **32**(4), 363–403.

Laufer, J., 1949: Investigation of turbulent flow in a two-dimensional channel. National Advisory Commission on Aeronaut Technology Rep. 1053, 20 pp. [Available from California Institute of Technology, Pasadena, CA 91125.]

LeBlond, P., 1983: The Strait of Georgia: Functional anatomy of a coastal sea. *Can. J. Fish. Aquat. Sci.,* **40,** 1033–1063.

Leibovich, S., 1983: The form and dynamics of Langmuir circulations. *Annu. Rev. Fluid Mech.,* **15,** 391–427.

Li, M., and C. Garrett, 1993: Cell merging and the jet/downwelling ratio in Langmuir circulation. *J. Mar. Res.,* **51,** 737–769.

——, and ——, 1997: Mixed layer deepening due to Langmuir circulations. *J. Phys. Oceanogr.*, **27,** 121–132.

McNeil, C., 1995: A study of dissolved gaseous oxygen and nitrogen fluxes in the upper ocean. Ph.D. thesis, University of Victoria, 159 pp. [Available from Institute of Ocean Science, P.O. Box 6000, Sidney, BC V8L 4B2 Canada.]

McPhee, M., and J. Smith, 1976: Measurements of the turbulent boundary layer under pack ice. *J. Phys. Oceanogr.*, **6,** 696–711.

McWilliams, J., P. Sullivan, and C. Moeng, 1997: Langmuir turbulence in the ocean. *J. Fluid Mech.*, **334,** 1–30.

Mellor, G. L., and T. Yamada, 1982: Development of a turbulence closure model for geophysical fluid problems. *Rev. Geophys. Space Phys.*, **20,** 851–875.

Melville, W., 1996: The role of surface wave breaking in air-sea interaction. *Annu. Rev. Fluid Mech.*, **28,** 279–321.

Phillips, O., 1985: Spectral and statistical properties of the equilibrium range in wind-generated gravity waves. *J. Fluid Mech.*, **156,** 505–531.

Price, J. F., R. A. Weller, and R. Pinkel, 1986: Diurnal cycling: Observations and models of the upper ocean response to diurnal heating, cooling, and wind mixing. *J. Geophys. Res.*, **91,** 8411–8427.

Skyllingstad, E., and D. Denbo, 1995: An ocean large-eddy simulation of Langmuir circulations and convection in the surface mixed layer. *J. Geophys. Res.*, **100,** 8501–8522.

Smith, S., R. Anderson, W. Oost, C. Kraan, N. Maat, J. DeCosmo, K. Katsaros, K. Davidson, K. Bumke, L. Hasse, and H. Chadwick, 1992: Sea surface wind stress and drag coefficients: The HEXOS results. *Bound.-Layer Meteor.*, **60,** 109–142.

Vagle, S., and D. Farmer, 1992: The measurement of bubble size distribution by acoustical backscatter. *J. Atmos. Oceanic Technol.*, **9,** 630–644.

Weller, R., and J. F. Price, 1988: Langmuir circulation within the oceanic mixed layer. *Deep-Sea Res.*, **35,** 711–747.

——, R. Payne, W. Large, and W. Zenk, 1983: Wind measurements from an array of oceanographic moorings and from the F/S *Meteor* during JASIN 1978. *J. Geophys. Res.*, **88,** 9689–9705.